RESEARCH ARTICLE

WILEY

A phase-field based model for coupling two-phase flow with the motion of immersed rigid bodies

Martin Reder[1,2] │ **Paul W. Hoffrogge[2]** │ **Daniel Schneider[1,2]** │ **Britta Nestler[1,2]**

[1]Institute of Digital Materials Science, Karlsruhe University of Applied Sciences, Karlsruhe, Germany

[2]Institute of Applied Materials–Microstructure Modelling and Simulation, Karlsruhe Institute of Technology (KIT), Karlsruhe, Germany

Correspondence
Martin Reder, Institute of Digital Materials Science, Karlsruhe University of Applied Sciences, Moltkestraße 30, 76133 Karlsruhe, Germany.
Email: martin_dominik.reder@h-ka.de

Abstract

The interaction of immersed rigid bodies with two-phase flow is of high interest in many applications. A model for the coupling of a Hohenberg–Halperin type model for two-phase flow and a fictitious domain method for consideration of rigid bodies is introduced leading to a full multiphase-field method to address the overall problem. A normalized phase variable is used alongside a method for application of wetting boundary conditions over a diffuse fluid-solid interface. This enables the representation of capillary effects and different wetting behavior based on Young's law. A number of simulations is conducted in order to validate the model and highlight its ability to handle a variety of setups for two-phase particulate flow. This includes dynamic wetting situations, the motion of multiple particles within the two-phase flow and the interaction with arbitrarily shaped solid structures inside the domain.

KEYWORDS

contact, finite difference methods, fluid-solid systems, fluid-structure interaction, Navier–Stokes

1 │ INTRODUCTION

Problems involving the interaction of immiscible two-phase flow with solid bodies are encountered in many natural processes and technical applications. This includes marine engineering,[1] particles immersed in emulsions,[2] micro particle injection into a melt during the steel-making process[3] as well as slurry mixing and transport for example, during the manufacturing process of battery electrodes.[4] The numerical simulation of such problems is very challenging, since both a proper handling for two-phase flow and the fluid-solid interaction is required. Additionally, a method for tracking of the moving interfaces between those phases is required.

For the modeling of rigid body motion within fluid flow, different approaches exist for example, such with a body fitted mesh[5,6] or fictitious domain methods.[7,8] The latter ones employ a ghost fluid in the solid domain and ensure the rigid body motion via a body force added in the equations for the ghost fluid. One example of such a method is the distributed Lagrange multiplier (DLM) method of Sharma and Patankar.[9] A phase-field formulation of this DLM method is introduced in Reference 10.

The phase-field method is also well established for the treatment of multiphase and capillary flow.[11-13] This goes back to Hohenberg and Halperin,[14] who formulated a model, that couples the Navier–Stokes system with a Cahn–Hilliard

equation. This is also referred to as model H, which captures the dynamic of the free surface as well as the triple line at solid walls by the application of corresponding boundary conditions.[15] However, the coupling with moving solid bodies is not straightforward.

To address the combination of two-phase flow with suspended bodies, diffuse interface approaches in a full Eulerian configuration were presented for example, in the work of Malvandi et al.[16] or Calderer et al..[1] Both models are based on the level-set approach for surface tracking and the immersed boundary method for treatment of rigid body motion. Aland et al.[17] employ a phase-field method for representation of the solid as well as the two fluids. However, their model to capture rigid body motion comes with limitations, since it neglects rotation and is not quantitatively investigated, thus its accuracy cannot be assessed. All these approaches are not capable of modeling different wetting scenarios, since they assume perpendicular contact of free surfaces at the fluid-solid interface.

Other existing works utilize a phase-field method for the two-phase flow interacting with solid bodies, which allows incorporation of different wetting behavior. Joshi and Jaiman[18] combine an Allen–Cahn approach with the arbitrary Lagrange–Euler (ALE) method for the treatment of suspended solid bodies. Choi and Anderson[2] employ a Cahn–Hilliard model in conjunction with the extended finite element method (XFEM) and an ALE-scheme. Li et al.[19] propose a ternary Cahn–Hilliard model with Lagrangian patches to track the solid. Such approaches need a separate configuration and sophisticated numerical treatment to capture the fluid-solid interaction.

Within this work a multiphase-field approach is presented, which allows the coupling of rigid particulate flow with a two-phase fluid and enables the modeling of various wetting conditions. A similar method to Aland et al.[20] is used in order to apply wetting boundary conditions for the model H over a diffuse fluid-solid region. This follows the general approach of Li et al.[21] to apply boundary conditions via a diffuse interface. While Aland et al.[20] only consider fixed solids or such with prescribed motion, our method allows to couple the model H for two-phase flow with the phase-field DLM method from[10] to treat rigid body dynamics. This is achieved by using a normalization procedure. It enables to employ the rigid body projection method without changes compared to the single fluid case. The model H solution including the wetting boundary conditions is executed after the rigid body algorithm.

The presented model yields a full multiphase-field approach to cover both the parameterization of the two-phase flow and the immersed bodies while tracking the corresponding interfaces implicitly. Therefore, an Eulerian configuration is considered, where no restriction regarding the grid for spatial discretization arises. Thus, geometry fitted meshes are not required and since a time independent grid can be employed, there is no need for remeshing. Herein, the discretization is performed on a Cartesian grid, which avoids complex mesh generation and offers the potential to employ multigrid solvers efficiently for example, for the pressure Poisson equation. Additionally, a parallelization via domain decomposition is enabled straightforward and can be implemented using message passing interface (MPI).

The article is organized as follows. First, the treatment of the rigid particulate flow and the two phase-flow is presented within a phase-field formulation. A normalization procedure is introduced, that allows the decoupling of the two-phase flow problem on one hand and the particulate flow on the other. The latter one is treated with the phase-field DLM, which can be used without further adjustments compared to the single-fluid case. For the two-phase flow, the model H is formulated with respect to a normalized phase variable. Together with the knowledge of the rigid body motion obtained by the DLM method, the overall phase-field can be reconstructed.

The wetting behavior on the fluid-solid interface is covered following the approach of Aland et al..[20] Thereby, the general formalism of Li et al.[21] is adopted to apply the model H wetting boundary conditions over a diffuse fluid-solid interface. Therefore, the impact of a solid body or structure onto the fluid-fluid interface is properly represented. Thus triple line dynamics are captured with respect to the wetting behavior of the solid surface.

2 | MATHEMATICAL FORMULATION

2.1 | Rigid particulate flow model

The coupling of fluid flow with rigid body motion is achieved by the phase-field formulation of the DLM method from Reference 10. The model is briefly discussed here. It is based on a phase-field method for the parameterization of rigid body geometries. Therefore, the phase variable $\varphi_\alpha(\boldsymbol{x}, t) \in [0, 1]$ is introduced. It represents an order parameter, which can be viewed as the local volume fraction of a phase α at time t and a spatial point $\boldsymbol{x}$. Let N be the number of all occurring phases, that can be fluid or rigid bodies. All rigid bodies are represented by a ghost fluid, where an additional body force $\boldsymbol{f}^{\mathrm{rigid}}$ is introduced, that enforces rigid body motion in the corresponding domain. Thus the rigid particulate flow problem

is described according to the Navier–Stokes like equation system

$$\rho\dot{\boldsymbol{u}} = -\nabla p + \nabla \cdot \left[\mu\left(\nabla\boldsymbol{u} + \nabla^{\mathsf{T}}\boldsymbol{u}\right)\right] + \rho\boldsymbol{f}_{\mathrm{V}} - \nabla \cdot \boldsymbol{\Theta} + \rho\boldsymbol{f}^{\mathrm{rigid}}, \tag{1a}$$

$$\nabla \cdot \boldsymbol{u} = 0 \tag{1b}$$

containing the momentum Equation (1a) and the continuity Equation (1b) for incompressible flow. Herein $\boldsymbol{u}$ denotes the velocity field, $(\dot{\cdot}) = \partial_t(\cdot) + \nabla(\cdot)\boldsymbol{u}$ the material time derivative, ρ the mass density, p the pressure, μ the dynamic viscosity and $\boldsymbol{f}_{\mathrm{V}}$ a body force, for example, gravity. Note, that these equations are solved for the total fluid region Ω_{f} as well as for the ghost fluids Ω_{p}, which represent the rigid bodies $p = 1 \ldots N^{\mathrm{s}}$, where N^{s} denotes the number of solid phases. A schematic sketch of the different domains is given in Figure 1. The body force $\boldsymbol{f}^{\mathrm{rigid}}$ vanishes in the fluid region Ω_{f}. For points $\boldsymbol{x} \in \Omega_p$ inside a bodies domain, it acts as a Lagrange multiplier enforcing the symmetric part of the velocity gradient to vanish, which corresponds to rigid body motion. Due to this rigidity constraint, the viscous term does not contribute in the solid region irrespective of the choice of viscosity for the ghost fluid. The capillary tensor $\boldsymbol{\Theta}$ depends on the order parameter and its gradient and will be specified later. The mass density and the dynamic viscosity in diffuse interface regions are retrieved by a linear interpolation of the phase wise constant values ρ_α and μ_α via

$$\rho(\boldsymbol{x}, t) = \sum_{\alpha=1}^{N} \rho_\alpha \varphi_\alpha(\boldsymbol{x}, t) \quad \text{and} \quad \mu(\boldsymbol{x}, t) = \sum_{\alpha=1}^{N} \mu_\alpha \varphi_\alpha(\boldsymbol{x}, t). \tag{2}$$

Note, that for phase dependent densities, this formulation corresponds to a quasi-incompressible modeling of multiphase flow according to Ding et al.[22] This is an approximation, which formally is not guaranteed to fulfill thermodynamic dissipation inequalities, but is justified for small density contrasts. However, the more general formulation proposed by Abels et al.[12] can also be employed in conjunction with this DLM method without any restrictions.

In order to obtain $\boldsymbol{f}^{\mathrm{rigid}}$, two steps are performed. First the Navier–Stokes system (1) is solved without the Lagrange multiplier term via time integration over a specific time interval. This yields already the new velocity inside the fluid while in the solid region it gives rise to a preliminary velocity field $\boldsymbol{u}^*$, which does not represent a rigid body motion yet, but fulfills the momentum balance. Thus the preliminary velocity is used to calculate the momentum $\boldsymbol{p}_p$ and the angular momentum $\boldsymbol{L}_p$ of the pth rigid body via

$$\boldsymbol{p}_p := m_p\boldsymbol{U}_p = \int_{\Omega_p} \rho\boldsymbol{u}^* \, \mathrm{d}V, \tag{3a}$$

$$\boldsymbol{L}_p := \boldsymbol{J}_p\boldsymbol{\omega}_p = \int_{\Omega_p} \rho(\boldsymbol{x} - \boldsymbol{x}_p) \times \boldsymbol{u}^* \, \mathrm{d}V, \tag{3b}$$

where m_p is the mass of the body, $\boldsymbol{J}_p$ its rotational inertia, $\boldsymbol{U}_p$ the barycenter velocity, $\boldsymbol{\omega}_p$ the angular velocity, $\boldsymbol{x}_p$ the barycenter and Ω_p the volume occupied by the pth body. The Equations (3) allow to calculate $\boldsymbol{U}_p$ and $\boldsymbol{\omega}_p$, which can be used to retrieve the actual rigid body velocity field

$$\boldsymbol{u}_p = \boldsymbol{U}_p + \boldsymbol{\omega}_p \times (\boldsymbol{x} - \boldsymbol{x}_p), \qquad \forall \boldsymbol{x} \in \Omega_p. \tag{4}$$
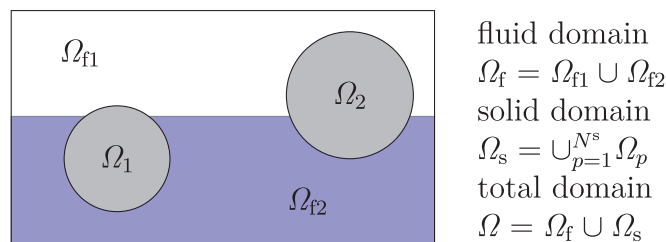

FIGURE 1 Sketch of the different domains for a two-phase particulate flow problem. In context of the phase-field method, the sharp interfaces between the domains are replaced by diffuse transition regions

In the diffuse interface formulation of the DLM, the integrals over each body are approximated via $\int_{\Omega_p}(\cdot)\,dV \approx \int_{\Omega}\varphi_p(\cdot)\,dV$, where φ_p represents the phase variable of the pth rigid body. In the fluid-body interface, the velocity field is retrieved via linear interpolation of the fluid and rigid body velocity and thus the overall solution for a new time step t_{n+1} is obtained by

$$\boldsymbol{u}^{n+1} = \varphi^{\mathrm{f}}\boldsymbol{u}^* + \sum_{p=1}^{N^{\mathrm{s}}}\varphi_p\boldsymbol{u}_p, \tag{5}$$

where φ^{f} is the phase variable of the fluid. Please note, that this projection violates the momentum preservation in a diffuse interface formulation. Thus an additional correction step is applied, which is discussed in Reference 10. Additionally, the rigid body projection method is complemented by a collision model to treat contact of different rigid particles or between particles and a static arbitrary solid structure within the flow. Further details of the algorithm employed for the particulate flow are found in Reference 10. It also contains a validation and convergence study of the rigid body model within a single fluid.

The phase variable φ_p of a rigid body can generally be determined by a shape preserving Allen–Cahn type equation (details see e.g., Reference 23). In the special case of spherical bodies it can directly be prescribed using a known equilibrium profile for example, via

$$\varphi_p(\eta_p) = \begin{cases} \frac{1}{2}\left[1 - \sin\left(\frac{\pi\eta_p}{\delta_{\mathrm{fs}}}\right)\right] & -\delta_{\mathrm{fs}}/2 \leq \eta_p \leq \delta_{\mathrm{fs}}/2 \\ 0 & \eta_p > \delta_{\mathrm{fs}}/2 \\ 1 & \eta_p < -\delta_{\mathrm{fs}}/2 \end{cases} \tag{6}$$

with the interface normal co-ordinate $\eta_p(\boldsymbol{x},t) = \|\boldsymbol{x} - \boldsymbol{x}_p(t)\| - R$ pointing from solid to fluid, the particle radius R and the fluid-solid interface thickness δ_{fs} as depicted in Figure 2.

2.2 | Two-phase flow model

A well-established model for two-phase flow in context of a phase-field method is the Hohenberg and Halperin[14] type model, also referred to as model H. The Navier–Stokes system (1) is augmented with an evolution equation for one of the two fluid phases, the other one is retrieved by the summation constraint $\varphi_1^{\mathrm{f}} + \varphi_2^{\mathrm{f}} = 1$, that holds, when only the two fluids are present. The evolution equation can either be of Cahn–Hilliard type[11] or the volume preserving Allen–Cahn equation. A comparison and discussion on both choices may be found in Gal and Medjo.[24] The fluid-solid coupling proposed in this article is not restricted to one of the formulations and can be derived for both. Subsequently, we consider a two-phase flow model based on the Cahn–Hilliard formulation. For both fluids the respective Cahn–Hilliard equation describes their evolution. Due to the summation constraint, only one equation needs to be considered, which reads

$$\dot{\varphi} = \kappa\nabla^2\Phi, \tag{7a}$$

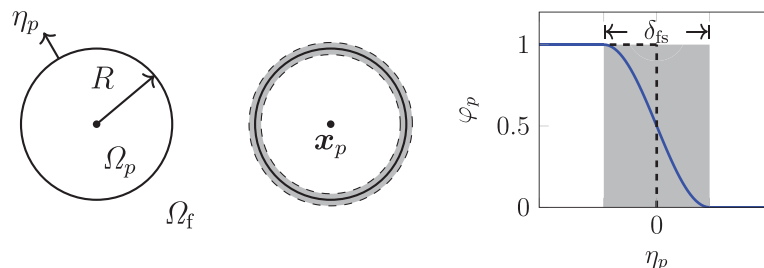$$\Phi = a_2\partial_\varphi\psi(\varphi) - a_1\nabla^2\varphi, \tag{7b}$$

FIGURE 2 Parameterization of a spherical rigid body. Left: Sharp interface. Middle: Diffuse interface representation. Right: Profile of the phase variable according to Equation (6)

using the abbreviation $\varphi = \varphi_1^{\mathrm{f}}$. Herein, $\boldsymbol{\Phi}$ is the chemical potential, κ a mobility coefficient and $\psi(\varphi)$ is a free energy potential. The coefficients a_1 and a_2 take the form

$$a_1 = k_1 \sigma \epsilon, \tag{8}$$

$$a_2 = k_2 \frac{\sigma}{\epsilon}, \tag{9}$$

where σ is the surface energy density between both fluids, ϵ a parameter describing the width of the fluid-fluid interface and k_1 and k_2 dimensionless constant prefactors, that depend on the choice of ψ and the cut-off definition of the interface in case of an asymptotic profile.[11] The fluid-fluid interface is implicitly given via

$$\Gamma_{\mathrm{ff}} = \{\boldsymbol{x} \in \Omega \; : \; \varphi_1^{\mathrm{f}} = 0.5\} \tag{10}$$

and thus corresponds to the 0.5-iso-surface. Subsequently, we employ the double-well potential $\psi(\varphi) = \varphi^2(1-\varphi)^2$ and the constants $k_1 = 1$, $k_2 = 18$ leading to the chemical potential

$$\boldsymbol{\Phi} = \frac{36\sigma}{\epsilon} \varphi(2\varphi^2 - 3\varphi + 1) - \sigma\epsilon\nabla^2\varphi \tag{11}$$

and the equilibrium phase-field profile

$$\varphi(\eta) = \frac{1}{2}\left[1 - \tanh\left(\frac{3\eta}{\epsilon}\right)\right], \tag{12}$$

where η denotes the normal co-ordinate of the fluid-fluid interface Γ_{ff} defined as

$$\eta(\boldsymbol{x}, t) = \min_{\boldsymbol{x}' \in \Gamma_{\mathrm{ff}}(t)} \|\boldsymbol{x} - \boldsymbol{x}'\|. \tag{13}$$

Equation (12) represents an asymptotic profile and thus no finite interface width δ_{ff} can be defined. However, a cut-off to 1 and 0 is used at $\eta = \pm\epsilon$, which yields an interface width of $\delta_{\mathrm{ff}} = 2\epsilon$. Within the diffuse fluid-fluid interface this leads to the equilibrium profile

$$\varphi(\eta) = \frac{1}{2}\left[1 - \tanh\left(\frac{6\eta}{\delta_{\mathrm{ff}}}\right)\right], \qquad -\delta_{\mathrm{ff}}/2 \leq \eta \leq \delta_{\mathrm{ff}}/2. \tag{14}$$

The values for cutting are $\varphi^- = [1 - \tanh(3)]/2 \approx 0.00247$ and $\varphi^+ = [1 + \tanh(3)]/2 \approx 0.99753$, respectively. The finite interface width resulting from the cut-off can be exploited to save computational cost in the implementation since a lot of calculations can be simplified or omitted in bulk regions. Note, that the cut-off can lead to the loss of phase preservation for the Cahn–Hilliard equation. The introduced error depends on the mobility and spatial resolution. It vanishes in the limit $\delta_{\mathrm{ff}} \to 0$ and $\kappa \to 0$. Thus, the cut is justified only for low mobilities and reasonable resolution, which we ensured within this work. The volume deviation between the simulation start and end time was below 0.5% in all cases. According to Jacqmin,[11] the mobility of the Cahn–Hilliard equation should be chosen as

$$\kappa \propto (\delta_{\mathrm{ff}})^p,$$

where p is restricted between 1 and 2. Thus the mobility goes to zero in the sharp interface limit yielding a purely convective transport equation for the phase-field. A value of $p = 1.9$ is used in this work for varying interface thickness for example, in case of a grid refinement.

The capillary tensor in the momentum Equation (1a) can be calculated via

$$\boldsymbol{\Theta} = a_1 \left(\nabla\varphi \otimes \nabla\varphi\right) = a_1 \|\nabla\varphi\|^2 \left(\boldsymbol{n} \otimes \boldsymbol{n}\right). \tag{15}$$

The capillary term accounts for curvature minimization effects due to surface tension. It only arises in the fluid-fluid interface, since $\nabla\varphi = \boldsymbol{0}$ holds otherwise. The interface normal vector is defined via $\boldsymbol{n} = \nabla\varphi/\|\nabla\varphi\|$. Note, that in literature

different representations of the capillary term can be found for example, the stress tensor $a_1(\nabla\varphi \otimes \nabla\varphi - \nabla\varphi \cdot \nabla\varphi \mathbf{1})$ or the potential form, that uses $\varphi\nabla\Phi$ instead of $\nabla \cdot \boldsymbol{\Theta}$ in the Navier–Stokes equation.[13] The representations only differ in the spherical part of capillary stresses, which is compensated by the pressure due to enforced incompressibility and thus the formulations are analytically equivalent. In the numerical implementation, the potential form behaves better for equilibrating problems, whereas the stress formulations are good in more dynamic situations (details see Jacqmin[25]).

2.3 | Normalization procedure for the fluid phases

We now aim to employ the model H for two-phase flow together with the rigid body projection by subdividing the overall problem into subproblems for the two-phase flow on one hand and the rigid particulate flow on the other. Decoupling both problems in this way allows to use the rigid body model without any adjustments. Therefore considering more than one fluid does not change the rigid body algorithm compared to the single fluid case. The decoupling is achieved by the introduction of a normalized order parameter for two-phase flow in conjunction with a proper coupling for the fluid-solid interface region. A multiphase problem is considered, which consists of N^{f} fluid phases and N^{s} solid phases, that can either be rigid bodies immersed in the flow or some stationary obstacle structure. The total number of occurring phases is $N = N^{\mathrm{f}} + N^{\mathrm{s}}$. The phase variable φ_α can be interpreted as the local volume fraction of phase α inside an infinitesimal representative volume element (RVE) of volume V and thus we have

$$\varphi_\alpha = \frac{V_\alpha}{V} \tag{16}$$

with the summation constraint

$$\sum_{\alpha=1}^{N} \varphi_\alpha = 1. \tag{17}$$

It is convenient to define the volume fractions of total fluid and solid phases by

$$\varphi^{\mathrm{f}} = \frac{V^{\mathrm{f}}}{V} = \sum_{q=1}^{N^{\mathrm{f}}} \varphi_q^{\mathrm{f}} \quad \text{and} \quad \varphi^{\mathrm{s}} = \frac{V^{\mathrm{s}}}{V} = \sum_{p=1}^{N^{\mathrm{s}}} \varphi_p^{\mathrm{s}}, \tag{18}$$

respectively. With this, the summation constraint yields

$$\varphi^{\mathrm{f}} + \varphi^{\mathrm{s}} = 1. \tag{19}$$

In order to decouple the fluid and the solid problem, a normalization is performed, which leads to a modified phase variable representing the volume fraction of a fluid q based on the total fluid volume

$$\tilde{\varphi}_q^{\mathrm{f}} := \frac{V_q^{\mathrm{f}}}{V^{\mathrm{f}}} = \frac{\varphi_q^{\mathrm{f}}}{\varphi^{\mathrm{f}}}, \quad \text{for} \quad \varphi^{\mathrm{f}} > 0 \tag{20}$$

and analogously for the solid phases. With respect to these normalized variables, both the fluid and the solid subproblem can be considered as a separate multiphase system. In particular we have summation constraints with regards to the normalized variables, which in the fluid case reads as

$$\sum_{q=0}^{N^{\mathrm{f}}} \tilde{\varphi}_q^{\mathrm{f}} = 1. \tag{21}$$

The evolution of a fluid phase q under a given solid phase change, that is determined by the motion of the rigid bodies, is obtained from Equation (20) as

$$\partial_t \varphi_q^{\mathrm{f}} = \varphi^{\mathrm{f}} \, \partial_t \tilde{\varphi}_q^{\mathrm{f}} + \tilde{\varphi}_q^{\mathrm{f}} \, \partial_t \varphi^{\mathrm{f}}, \tag{22}$$

where due to Equation (19)

$$\partial_t \varphi^f = -\partial_t \varphi^s = \sum_{p=0}^{N^s} \partial_t \varphi_p^s \qquad (23)$$

holds. Subsequently, a two-phase fluid is considered, which allows the employment of a single order parameter for the fluid-fluid subproblem since the other one is determined by the summation constraint (21). Therefore, the abbreviation $\tilde{\varphi} := \tilde{\varphi}_1^f$ is introduced. The temporal derivatives of both fluid phases are given via

$$\partial_t \varphi_1^f = \left(1 - \varphi^s\right) \partial_t \tilde{\varphi} - \tilde{\varphi} \partial_t \varphi^s, \qquad (24a)$$

$$\partial_t \varphi_2^f = -\left(1 - \varphi^s\right) \partial_t \tilde{\varphi} - (1 - \tilde{\varphi}) \partial_t \varphi^s. \qquad (24b)$$

In order to update both fluid phases, $\partial_t \tilde{\varphi}$ and $\partial_t \varphi^s$ need to be available. The latter is determined by rigid body motion. As soon as the rigid body velocity field $\boldsymbol{u}_p$ is known from Equation (4), we have

$$\partial_t \varphi^s = \sum_{p=1}^{N^s} \boldsymbol{u}_p \cdot \nabla \varphi_p, \qquad (25)$$

where $\nabla \varphi_p$ is obtained by Equation (6) for spherical particles or for example, from a shape preserving Allen–Cahn equation for general bodies. The Cahn–Hilliard equation (7a) is formulated in terms of the normalized phase variable, which yields

$$\partial_t \tilde{\varphi} = -\boldsymbol{u} \cdot \nabla \tilde{\varphi} + \kappa \nabla^2 \boldsymbol{\Phi}, \qquad (26a)$$

$$\boldsymbol{\Phi} = a_2 \partial_{\tilde{\varphi}} \psi(\tilde{\varphi}) - a_1 \nabla^2 \tilde{\varphi} \qquad (26b)$$

and therefore determines the time derivative $\partial_t \tilde{\varphi}$. This normalization procedure allows the separated treatment of two-phase flow on one hand and rigid particulate flow on the other as well as the reconstruction of all the original order parameters. Up to this point, the two-phase flow subproblem does not yet include the influence of solid bodies by means of wetting behavior. The consideration of this coupling is addressed in the subsequent section.

2.4 | Coupling at the fluid-solid interface

In order to correctly capture the triple line dynamics between the two fluid phases and a solid phase, appropriate boundary conditions need to be applied. Let Γ_{fs} be the sharp fluid-solid interface, which is in context of the phase-field method identified with the iso-surface

$$\Gamma_{fs} = \left\{ \boldsymbol{x} \in \Omega \ : \ \varphi^f = 0.5 \right\} \qquad (27)$$

and $\Gamma_{fs}^d = \left\{ \boldsymbol{x} \in \Omega \ : \ 0 < \varphi^f < 1 \right\}$ is defined as the diffuse fluid-solid interface. According to the literature,[11] the boundary conditions for modeling wetting of walls represented by a sharp fluid-solid interface are

$$\nabla \boldsymbol{\Phi} \cdot \boldsymbol{n}^f = 0, \qquad \forall \boldsymbol{x} \in \Gamma_{fs} \qquad (28)$$

and

$$a_1 \nabla \tilde{\varphi} \cdot \boldsymbol{n}^f = (\sigma_{2s} - \sigma_{1s}) \partial_{\tilde{\varphi}} h^{ff}, \qquad \forall \in \Gamma_{fs} \qquad (29)$$

with respect to the Cahn–Hilliard equation (26a). Herein $\boldsymbol{n}^f$ is the normal vector pointing from fluid to solid, σ_{1s} and σ_{2s} are the surface energy densities between the solid and the respective fluid. The interpolation function h^{ff} exhibits a monotonic transition between zero and unity. An evident choice would be $h^{ff} = \tilde{\varphi}$, but also other functions meeting the conditions specified in Reference 26 are appropriate. Higher order polynomials in $\tilde{\varphi}$ lead to a steeper transition of h^{ff} in
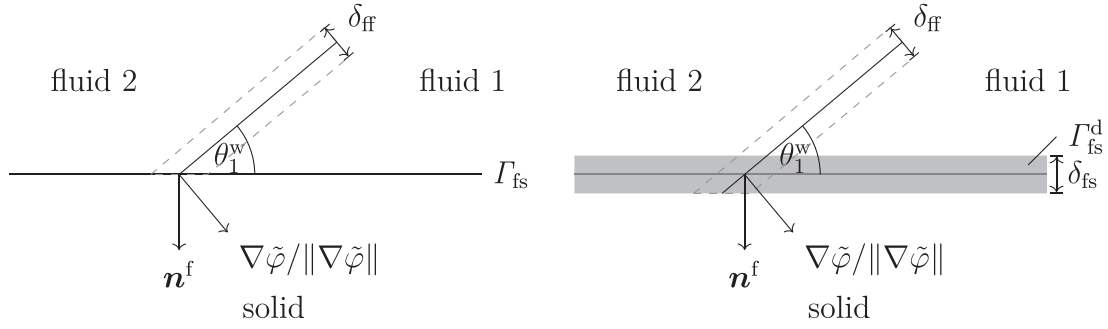
FIGURE 3 Contact angle at the triple line. Left: Sharp fluid-solid interface Γ_{fs}. Right: Diffuse fluid-solid interface $\Gamma_{\text{fs}}^{\text{d}}$

interface normal direction η. Within this article, we use $h^{\text{ff}} = \tilde{\varphi}^2(3 - 2\tilde{\varphi})$, which yields $\partial_{\tilde{\varphi}} h^{\text{ff}} = 6\tilde{\varphi}(1 - \tilde{\varphi})$. The boundary condition (29) reproduces the static contact angle according to Young's law. It can be rewritten to

$$\nabla\tilde{\varphi} \cdot \boldsymbol{n}^{\text{f}} = \frac{1}{k_1\varepsilon} \cos\theta_1^{\text{w}} \partial_{\tilde{\varphi}} h^{\text{ff}}, \tag{30}$$

where the cosine of the equilibrium contact angle between the first fluid and a solid according to Figure 3 is determined by

$$\cos\theta_1^{\text{w}} = \frac{\sigma_{2\text{s}} - \sigma_{1\text{s}}}{\sigma}. \tag{31}$$

At the boundary $\partial\Omega$ of the computational domain, these boundary conditions are applied directly in their discrete representation, which can be found in Appendix B.

However, for the fluid-solid interface Γ_{fs} inside the domain, for example, the surface of a rigid body, we aim to employ a diffuse fluid-solid interface. Thus the application of the boundary conditions is not straightforward like in case of a sharp fluid-solid interface. We use the approach introduced by Li et al.[21] in order to apply them as previously done in Reference 20. The detailed derivation can be found in Appendix A. By extension of the integration domain in its weak form, the Cahn–Hilliard boundary value problem for the fluid with a sharp fluid-solid interface can be formulated via

$$I\boldsymbol{\Phi} = a_2 I \partial_{\tilde{\varphi}} \psi - a_1 \nabla \cdot (I\nabla\tilde{\varphi}) - \delta_\Gamma(\sigma_{2\text{s}} - \sigma_{1\text{s}})\partial_{\tilde{\varphi}} h^{\text{ff}}, \tag{32a}$$

$$I\dot{\tilde{\varphi}} = \kappa\nabla \cdot (I\nabla\boldsymbol{\Phi}) \tag{32b}$$

with I being an indicator function of the fluid domain, which corresponds to the Heaviside function normal to Γ_{fs} and δ_Γ is the respective Dirac distribution. The diffuse interface approximation of this is done by approximating the indicator function via $I \approx h^{\text{fs}}(\varphi^{\text{f}})$ and the Dirac distribution via $\delta_\Gamma = \|\nabla I\| \approx \partial_{\varphi^{\text{f}}} h^{\text{fs}}(\varphi^{\text{f}})\|\nabla\varphi^{\text{f}}\|$ and thus

$$h^{\text{fs}}\boldsymbol{\Phi} = a_2 h^{\text{fs}} \partial_{\tilde{\varphi}} \psi - a_1 \nabla \cdot \left(h^{\text{fs}}\nabla\tilde{\varphi}\right) - \partial_{\varphi^{\text{f}}} h^{\text{fs}}\|\nabla\varphi^{\text{f}}\|(\sigma_{2\text{s}} - \sigma_{1\text{s}})\partial_{\tilde{\varphi}} h^{\text{ff}}, \tag{33a}$$

$$h^{\text{fs}}\dot{\tilde{\varphi}} = \kappa\nabla \cdot \left(h^{\text{fs}}\nabla\boldsymbol{\Phi}\right). \tag{33b}$$

The interpolation function h^{fs} does not necessarily need to be the same as h^{ff} for the fluid-fluid interface. However, within this article, we choose a similar interpolation function and thus $h^{\text{fs}} = (\varphi^{\text{f}})^2(3 - 2\varphi^{\text{f}})$. Note, that outside the diffuse fluid-solid interface, we have $\varphi^{\text{f}} = 1$, thus $\tilde{\varphi} = \varphi_1^{\text{f}}$ and the gradient $\nabla\varphi^{\text{f}}$ vanishes. Therefore, Equation (33) reduces to the classical Cahn–Hilliard equation in absence of solid phases.

3 | IMPLEMENTATION AND NUMERICAL TREATMENT

The equation system for the overall model is given as

$$\rho\dot{\boldsymbol{u}} = -\nabla p + \nabla \cdot \left[\mu\left(\nabla\boldsymbol{u} + \nabla^{\mathsf{T}}\boldsymbol{u}\right)\right] + \rho\boldsymbol{f}_{\text{V}} - \nabla \cdot \boldsymbol{\Theta} + \rho\boldsymbol{f}^{\text{rigid}}, \tag{34a}$$

$$\nabla \cdot \boldsymbol{u} = 0, \tag{34b}$$

$$\boldsymbol{u}_p = \boldsymbol{U}_p + \boldsymbol{\omega}_p \times (\boldsymbol{x} - \boldsymbol{x}_p), \tag{34c}$$

$$\boldsymbol{f}^{\mathrm{rigid}} = \begin{cases} 0 & \varphi^{\mathrm{s}} = 0 \\ \sum_{p=1}^{N^{\mathrm{s}}} \boldsymbol{f}_p^{\mathrm{rigid}}(\boldsymbol{u}_p, \boldsymbol{u}^*, \varphi_p) & \mathrm{otherwise} \end{cases}, \tag{34d}$$

$$h^{\mathrm{fs}}\boldsymbol{\Phi} = a_2 h^{\mathrm{fs}}\partial_{\tilde{\varphi}}\psi - a_1 \nabla \cdot \left(h^{\mathrm{fs}}\nabla\tilde{\varphi}\right) - \partial_{\varphi^{\mathrm{f}}}h^{\mathrm{fs}}\|\nabla\varphi^{\mathrm{f}}\|(\sigma_{2\mathrm{s}} - \sigma_{1\mathrm{s}})\partial_{\tilde{\varphi}}h^{\mathrm{ff}}, \tag{34e}$$

$$h^{\mathrm{fs}}\dot{\tilde{\varphi}} = \kappa \nabla \cdot \left(h^{\mathrm{fs}}\nabla\boldsymbol{\Phi}\right). \tag{34f}$$

For details on the projection method for the rigid body representation and thus the expression of $\boldsymbol{f}^{\mathrm{rigid}}$ we refer to Reference 10. The partial differential equations are solved using a finite difference method on a Cartesian grid. Some details on the discretization can be found in Section 3.3. An overview of the algorithm is given in Section 3.2.

3.1 | Treatment of pure solid regions

The normalized phase variable $\tilde{\varphi}$ is only defined in the fluid domain $\Omega_{\mathrm{f}>0} = \{\boldsymbol{x} \in \Omega \; : \; \varphi^{\mathrm{f}}(\boldsymbol{x}) > 0\}$. If the total fluid phase φ^{f} is zero, the definition of the modified phase variable becomes a singularity. However, the values of $\tilde{\varphi}$ must be known also in the purely solid regions $\Omega_{\mathrm{f}=0} = \{\boldsymbol{x} \in \Omega \; : \; \varphi^{\mathrm{f}}(\boldsymbol{x}) = 0\}$. For points, that have a value of $(\varphi^{\mathrm{f}})^n = 0$ at time t_n but become fluid points with $(\varphi^{\mathrm{f}})^{n+1} > 0$ at time t_{n+1}, $\tilde{\varphi}$ must be known in order to determine, how φ^{f} is split into φ_1^{f} and φ_2^{f}. Therefore, the normalized phase variable is extrapolated from the fluid domain $\Omega_{\mathrm{f}>0}$ into the nonfluid domain $\Omega_{\mathrm{f}=0}$. This is done with the linear extrapolation

$$\tilde{\varphi}(\boldsymbol{x}) = \min\left[\max\left[2\tilde{\varphi}(\boldsymbol{x} - c\boldsymbol{n}^{\mathrm{f}}) - \tilde{\varphi}(\boldsymbol{x} - 2c\boldsymbol{n}^{\mathrm{f}}), \, 0\right], \, 1\right], \quad \boldsymbol{x} \in \Omega_{\mathrm{f}=0}, \tag{35}$$

where $\boldsymbol{n}^{\mathrm{f}}$ is the outward pointing normal vector of the fluid and c is chosen to be the mean discretization step size $\sqrt{\Delta x \Delta y}$ or $\sqrt[3]{\Delta x \Delta y \Delta z}$ in 2D or 3D, respectively. The values of $\tilde{\varphi}(\boldsymbol{x} - c\boldsymbol{n}^{\mathrm{f}})$ and $\tilde{\varphi}(\boldsymbol{x} - 2c\boldsymbol{n}^{\mathrm{f}})$ are linearly interpolated from the respective grid positions. As a threshold to perform this extrapolation we choose $\varphi^{\mathrm{f}} < 0.05$ within this work.

3.2 | Algorithm for rigid bodies within two-phase flow

An overview of the algorithm, that is employed, is given below. More details regarding the Navier–Stokes solution and rigid body projection (steps 1.–3.) are found in Reference 10 and the algorithm overview, Section 2.6 therein. At the beginning of a time step t_n the quantities $\boldsymbol{x}_p^n, \boldsymbol{u}^n, \boldsymbol{U}_p^n, \varphi_1^n, \dots, \varphi_N^n$ are known.

1. Calculate the Navier–Stokes solution (1) explicitly to obtain $\boldsymbol{u}^*$.
2. Perform the rigid body projection, which yields $\boldsymbol{U}_p^{n+1}$ and $\boldsymbol{u}^{n+1}$.
3. Check for particle collision and apply corresponding velocity corrections (details see Reference 10).
4. Update the rigid body position

$$\boldsymbol{x}_p^{n+1} = \boldsymbol{x}_p^n + \frac{\Delta t}{2}\left(\boldsymbol{U}_p^{n+1} + \boldsymbol{U}_p^n\right).$$

5. Set the modified phase variable at time t_n via

$$(\tilde{\varphi})^n = \left(\frac{\varphi_1^{\mathrm{f}}}{\varphi^{\mathrm{f}}}\right)^n \quad \mathrm{for} \quad (\varphi^{\mathrm{f}})^n > 0.$$

6. Extrapolate $\tilde{\varphi}$ into regions with $(\varphi^{\mathrm{f}})^n = 0$ using Equation (35).
7. Calculate $\Delta\tilde{\varphi} = \tilde{\varphi}^{n+1} - \tilde{\varphi}^n$ via Equation (33) for $\boldsymbol{x} \in \Omega_{\mathrm{f}>0}$.

8. For each point $x \in \Omega$

(a) Determine the change of solid phase

$$\Delta \varphi^{\mathrm{s}} = \sum_{p=1}^{N^{\mathrm{s}}} \varphi_p \left(x, x_p^{n+1} \right) - \left(\varphi_p^{\mathrm{s}} \right)^n$$

using Equation (6) and update the solid phase variables φ_p^{s}.

(b) Update the fluid phase variables via

$$\left(\varphi_1^{\mathrm{f}} \right)^{n+1} = (1 - \varphi^{\mathrm{s}})^{n+1} \Delta \tilde{\varphi} - \tilde{\varphi}^{n+1} \Delta \varphi^{\mathrm{s}} + \left(\varphi_1^{\mathrm{f}} \right)^n,$$

$$\left(\varphi_2^{\mathrm{f}} \right)^{n+1} = -(1 - \varphi^{\mathrm{s}})^{n+1} \Delta \tilde{\varphi} - (1 - \tilde{\varphi}^{n+1}) \Delta \varphi^{\mathrm{s}} + \left(\varphi_2^{\mathrm{f}} \right)^n.$$

3.3 | Numerical discretization

The presented model is implemented within the PACE3D-code,[27] which is a multiphysics framework based on the multiphase-field method. The partial differential equations are solved on a Cartesian grid using a finite difference method in conservation form. The time integration is done by means of the explicit Euler method and thus the method is first order accurate in time. A Chorin-type projection method is employed for solution of the Navier–Stokes system. Therefore, a staggered grid arrangement is used, where the velocity components are located at a cells' face center in the corresponding direction. The pressure as well as the phase-field order parameters are located at the cell centers. The Cahn–Hilliard equation and the Poisson equation for the pressure use grid cells as control volume, while for the momentum balance the control volume is shifted by half the discretization step size in the corresponding direction. The Poisson equation is solved with a conjugated gradient method and a Gauß–Seidel coarse grid preconditioning with one fourth the resolution of the original grid. A residual of 1×10^{-8} is used for exiting the iterative solution process.

The spatial discretization is shown exemplarily by specifying it for the x-component of some terms. Let i be the index of a cell center and u the x-component of the velocity field, then the viscous term at the face center $i + 1/2$ is discretized via

$$\left[\frac{1}{\rho} \partial_x(\mu \partial_x u) \right]_{i+1/2} \approx \frac{1}{\rho(\varphi_{i+1/2})\Delta x} \left(f_{i+1}^{\mathrm{diff}} - f_i^{\mathrm{diff}} \right) \tag{36}$$

with the flux

$$f_i^{\mathrm{diff}} = \mu(\varphi_i) \frac{u_{i+1/2} - u_{i-1/2}}{\Delta x}, \tag{37}$$

where density and viscosity are calculated using the arithmetic mean according to Equation (2). Linear interpolation is used to obtain the values of the order parameters at the required position for example, $\varphi_{i+1/2} = (\varphi_{i+1} + \varphi_i)/2$ for the face center value. A central difference scheme (CDS) is employed for the capillary term and the order parameters are linearly interpolated to the required positions. The convection term is treated by

$$\left[\partial_x(u^2) \right]_{i+1/2} \approx \frac{1}{\Delta x} \left(f_{i+1}^{\mathrm{conv}} - f_i^{\mathrm{conv}} \right), \tag{38}$$

and the blending

$$f_i^{\mathrm{conv}} = u_i^{\mathrm{c}} \left[(1 - \gamma)u_i^{\mathrm{c}} + \gamma u_i^{\mathrm{u}} \right]. \tag{39}$$

between central differences and the first order upwind scheme is used for the fluxes. Herein, the central and upwind approximations are

$$u_i^{\mathrm{c}} = \frac{1}{2} \left(u_{i+1/2} + u_{i-1/2} \right), \tag{40}$$

and

$$
u_i^{\mathrm{u}} =
\begin{cases}
u_{i-1/2} & u_i^{\mathrm{c}} \geq 0 \\
u_{i+1/2} & u_i^{\mathrm{c}} < 0
\end{cases},
\tag{41}
$$

respectively. The blending parameter γ is chosen in such a way, that the cell Reynolds number criterion is fulfilled, which is

$$
\gamma =
\begin{cases}
0 & Re_{\max}^{\mathrm{c}} \leq 1.8 \\
1 - 1.8/Re_{\max}^{\mathrm{c}} & \text{otherwise}
\end{cases}
\tag{42}
$$

with $Re_{\max}^{\mathrm{c}} = \max_{\Omega}(\rho u \Delta x/\mu)$. Thus the scheme tends as much toward CDS as stability allows. For $\gamma = 0$, the spatial discretization is formally second order accurate. If not stated differently, the blending factor γ yields a maximum value of zero during a simulation, which corresponds to pure CDS. The convective term in the Cahn–Hilliard equation is discretized with the total variation diminishing (TVD) flux limiter scheme OSPRE.[28]

4 | VALIDATION AND NUMERICAL EXPERIMENTS

4.1 | Wetting behavior for a planar fluid-solid interface

In order to validate the diffuse boundary condition applied via Equation (33), we consider the wetting behavior of a droplet on a flat plate. The equilibrium droplet shape is a circular segment that maintains a certain contact angle θ_1^{w} with the wall (see Figure 4).

Accordingly, the contact angle is related to the aspect ratio of a droplet via

$$
\theta_1^{\mathrm{w}} = 2 \arctan\left(\frac{2l_y}{l_x}\right)
\tag{43}
$$

as shown in Appendix C. A number of simulations is carried out and the results are compared to theory. The contact angle is calculated by Equation (43) with regards to the iso-line $\Gamma_{\mathrm{fs}} = \{\boldsymbol{x} \in \Omega \ : \ \varphi^{\mathrm{f}} = 0.5\}$, which is approximately determined using a secant method. A droplet of diameter D is placed onto a diffuse wall within a domain of size $2D \times 0.8D$. The model H is solved with respect to Equations (1) and (33) until a steady equilibrium state is reached. All simulations are performed for three theoretical contact angles of 60°, 90° and 120°, respectively.

A convergence study is conducted with the resolution $n_x \times n_y$ varying between 180×72 and 280×112 cells distributed over the domain. The thickness of the fluid-solid and fluid-fluid interface is chosen as $\delta_{\mathrm{fs}} = 5\Delta x$ and $\delta_{\mathrm{ff}} = 6\Delta x$, respectively. Thus the interface width is reduced proportionally to the increase in spatial resolution. For $n_x = 200$ the resulting shapes are exemplarily plotted in Figure 5. The deviation between simulation result and theoretical contact angle is plotted over the spatial resolution in the left graph of Figure 6. In all three cases a monotonic convergence is observed with increase in resolution. The deviation is smallest for the theoretical contact angle of 90°, while the other two cases show generally higher deviations. For the two highest resolutions, the deviation lies within a range of $\pm 1°$.

Additionally, the influence of the diffuse interface thickness δ_{fs} is investigated. Therefore, δ_{fs} is varied while a resolution of 220×88 cells and $\delta_{\mathrm{ff}} = 6\Delta x$ is maintained. The right graph of Figure 6 depicts the contact angle deviation as
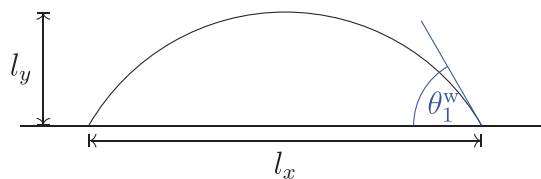
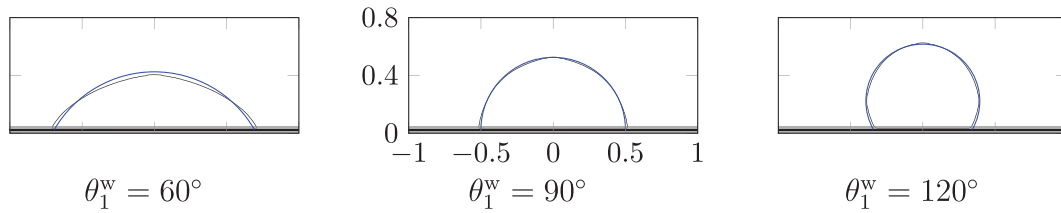FIGURE 4 Determination of the contact angle via $\tan(\theta_1^{\mathrm{w}}/2) = 2l_y/l_x$

FIGURE 5 Theoretical shape (blue) of the droplet and the simulation result (black) with diffuse fluid-solid interface for a resolution of 200×80 cells. The diffuse interface is plotted in gray, the wall is identified as Γ_{fs} and is located at $y = 0$
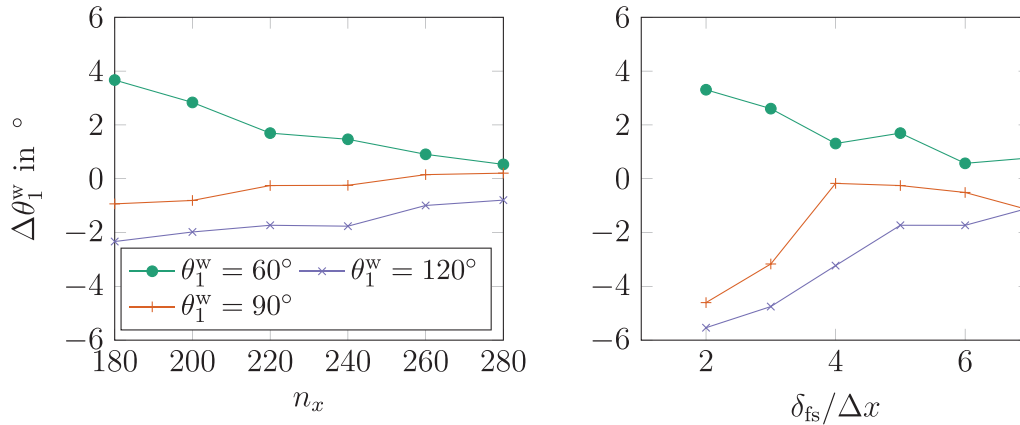

FIGURE 6 Deviation of the contact angle for varying interface thickness and grid resolution. Table C2 in the Appendix C contains the plot data. Left: Fixed number of six cells to resolve the interface. Right: Fixed grid with 220×88 cells

function of δ_{fs}. For a small thickness of the fluid-solid interface, large errors are occurring, which is due to an insufficient resolution of the interface. This leads to a poor approximation of the Dirac distribution and indicator function within Equation (33). For $\delta_{\mathrm{fs}} > 4\Delta x$, the deviation with respect to the theoretical value is within a range of $\pm 2°$. The simulation results with relatively fine grids and $\delta_{\mathrm{fs}} > 4\Delta x$ show an overall very good agreement with the theory.

4.2 | Heave decay of a body on a free surface

In this Section, we consider the heave motion of a floating sphere on a free surface of a fluid. The sphere is released from an initial height and floats under gravity g. For this setup Maskell and Ursell[29] derived an analytical solution for the linearized problem with neglected viscosity. Additionally, experimental data addressing this problem is available from Itō.[30] These results are subsequently used for validation. A sketch of the setup is depicted in Figure 7. The same set of parameters as in Reference 1 and 18 are chosen, which is $\rho_{\mathrm{f1}} = 1.2 \text{ kg m}^{-3}$, $\rho_{\mathrm{f2}} = 1000 \text{ kg m}^{-3}$, $\rho_{\mathrm{s}} = 500 \text{ kg m}^{-3}$, $\mu_{\mathrm{f1}} = 1.8 \times 10^{-5} \text{ kg m}^{-1}\text{s}^{-1}$, $\mu_{\mathrm{f2}} = 1 \times 10^{-3} \text{ kg m}^{-1} \text{ s}^{-1}$, $g = 9.81 \text{ ms}^{-2}$ and $D = 0.1524 \text{ m}$. The surface tension is $\sigma = 1.8 \times 10^{-6} \text{ kg s}^{-2}$ and thus capillary forces are negligible in this setup. A contact angle of $90°$ is considered at the fluid-solid interface. The time interval of the simulation is $0 \le t\sqrt{g/R} \le 20$. Simulations with two different resolutions are performed. The coarse grid has 2560×280 cells corresponding to $D/\Delta x = 46$, the number of time steps is 8000 and the mobility $\kappa = 0.07493 \text{ m}^3 \text{ s kg}^{-1}$. The fine grid has a refinement factor of 1.5. Thus 3840×420 cells, 12 000 time steps and the mobility $\kappa = 0.03468 \text{ m}^3 \text{ s kg}^{-1}$ is used. The interface thicknesses are chosen as $\delta_{\mathrm{ff}} = 8\Delta x$ and $\delta_{\mathrm{fs}} = 5\Delta x$. Therefore they are reduced proportionally to the refinement. The temporal development of the particle barycenter is plotted in Figure 8 for the theoretical and simulation result. Subsequently, the time is normalized with the constant ratio $\sqrt{g/R}$ representing a characteristic time scale.

The simulated particle shows an oscillating behavior, with an amplitude that decays quickly. In order to evaluate the deviations between the simulations and the theoretical solution, three different measures are used. The amplitude of the oscillation and the respective time difference in between is evaluated at each extremum. Averaging the relative
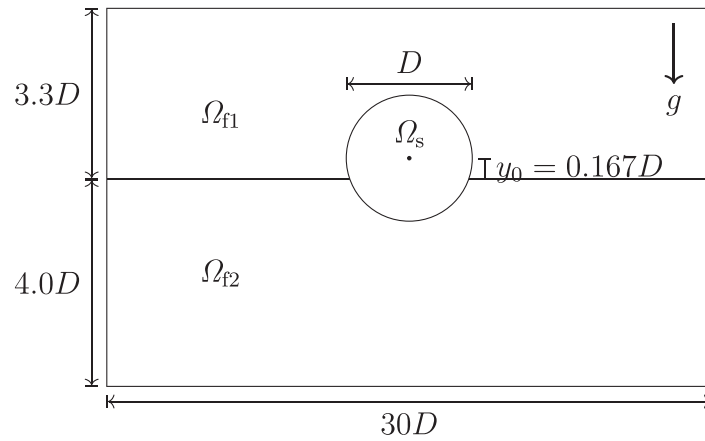
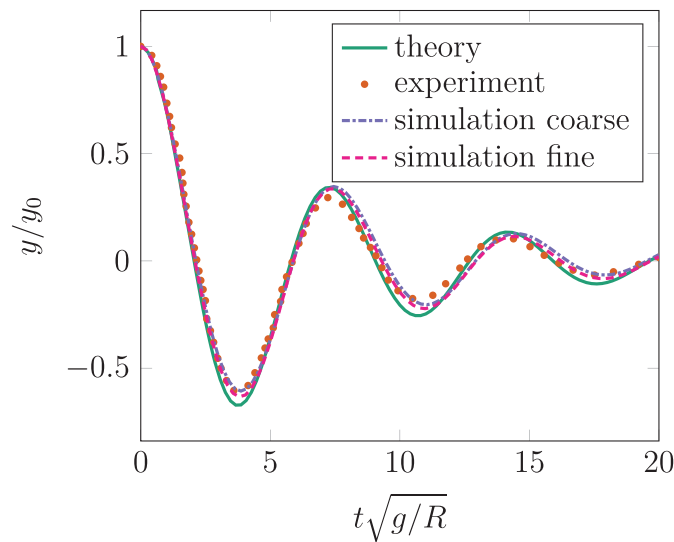**FIGURE 7** Initial setup for the heave decay problem

FIGURE 8 Normalized barycenter position y of the sphere over time. The time is normalized with the constant ratio $\sqrt{g/R}$. Comparison of the simulation result with the theoretical solution of Maskell and Ursell[29] and experiments of Itō[30]

deviation over all extrema yields the quantities e_a^{av} and e_T^{av} for amplitude and time difference, respectively. Additionally, the relative error by means of the L^2-norm is evaluated over the whole time interval. A comparison of these quantities is shown in Table 1. It can be seen, that both simulations yield an amplitude in between the theoretical and experimental results. The time difference between the extrema is slightly overestimated by the simulations, while the fine grid solution shows smaller deviations. Overall, considering that the deviation between experiment and theory is in the same order of magnitude, the results of simulation are in good agreement with both the theory and experimental results.

4.3 | Impact of a body on a free surface

Subsequently, the impact of a spherical body onto a fluid-fluid interface is considered as test case. The initial conditions are depicted in Figure 9. The domain boundary is considered as solid wall with 90° contact angle.

Within this setup we choose $D = 0.2$ m, $\rho_s = 20$ kg m^{-3} and $g = 4.69 \times 10^{-6}$ m s^{-2}. The parameters of both fluids are listed in Table 2 alongside the resulting Archimedes number $Ar = \rho(\rho_s - \rho)gD^3/\mu^2$, the Bond number $Bo = \rho g D^2/\sigma$, the Reynolds number $Re_\infty = \rho u_\infty D/\mu$, the Weber number $We_\infty = \rho u_\infty^2 D/\sigma$, and the capillary number $Ca_\infty = \mu u_\infty/\sigma$. Herein u_∞ is the stationary velocity of the body falling in the respective fluid. This is estimated employing the Schiller–Naumann

TABLE 1 Relative deviation between the simulation results with respect to the theoretical and experimental results as well as between the latter ones

	Coarse grid		Fine grid		
	Theory	Experiment	Theory	Experiment	Theory versus experiment
e_{L^2} in %	13.98	12.07	9.65	11.36	13.81
e_a^{av} in %	3.21	−2.13	2.46	−2.88	5.34
e_T^{av} in %	−7.76	−9.39	−6.52	−8.15	1.63

Note: The deviation e_{L^2} by means of the L^2-norm over the whole time span, the average amplitude error e_a^{av} and the average error in time difference between two extrema e_T^{av} are given.
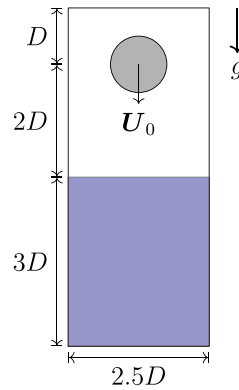
FIGURE 9 Initial setup for the impact on the free surface. The domain boundaries are walls with no slip condition and 90° contact angle

TABLE 2 Parameter of both fluids and resulting nondimensional numbers for the impact simulation

	ρ in $\frac{kg}{m^3}$	μ in $\frac{kg}{ms}$	σ in $\frac{kg}{s^2}$	Ar	Re_∞	Bo	Ca_∞	We_∞
Fluid 1	1	$1.8 \cdot 10^{-5}$	$5 \cdot 10^{-7}$	2200	41.6	0.3752	0.1346	5.5994
Fluid 2	15	$9.0 \cdot 10^{-5}$		347	10.9	5.6274	0.0588	0.6409

correlation,[31] which yields $Re_\infty = Ar/(18 + 2.7Re_\infty^{0.687})$ and thus an implicit equation to calculate u_∞. The initial velocity $U_0 = -u_{\infty,1}e_y$ of the body is applied. Simulations with three different contact angles between the body and fluid-fluid interface are performed, which are 60, 90, and 120°. The mobility is $\kappa = 0.0018$ m³ s kg⁻¹ and the spatial resolution is 200×480 cells. The interface thicknesses are $\delta_{ff} = 8\Delta x$ and $\delta_{fs} = 5\Delta x$.

The temporal development of the spherical particle's velocity and its barycenter location is depicted in Figure 10 for the three contact angles. According to Lee and Kim,[32] the impact behavior is driven by the dimensionless number $\iota := (\rho_{f2}/\rho_s)^2 We_{\infty,2}(Bo_2)^{3/2}$ as well as the contact angle on the solid surface. The present setup yields $\iota \approx 15$ and thus according to Reference 32, a sinking of the sphere is expected even in the 60° case, which is in agreement to the simulation results. The body's velocity decreases little before the impact with the denser fluid and drops rapidly afterwards. It approaches the theoretical stationary velocity $u_{\infty,2}$ before decreasing due to the wall's influence and finally vanishing, when contact occurs.

The temporal development of all three cases is almost identical up to the point, when the body is more than half immersed into the denser fluid. After this, the 90 and 120° case only show a minor difference, where the sinking is slightly faster for 120°, due to the wetting in favor of the denser fluid. The 60° case deviates significantly from the others, because of the larger contact area between fluid 1 and the body, which is favored by the wetting boundary condition and can be seen in the snapshots depicted in Figure 11. For $\theta_1^w = 60°$, a film of fluid 1 still remains after the full immersion of the body leading to a droplet adjacent to the body. This observation is in agreement with results from literature with similar
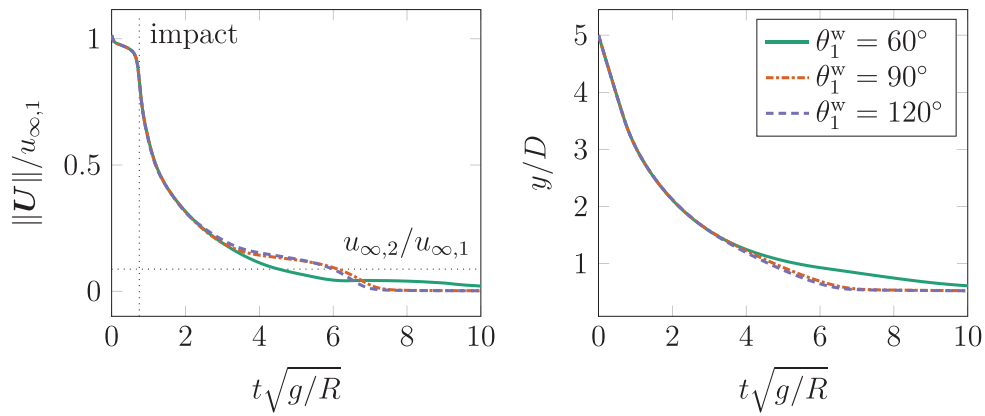
FIGURE 10 Time development of the particle velocity $\|U\|$ (left) and position (right) for the falling particle with different contact angles θ_1^w
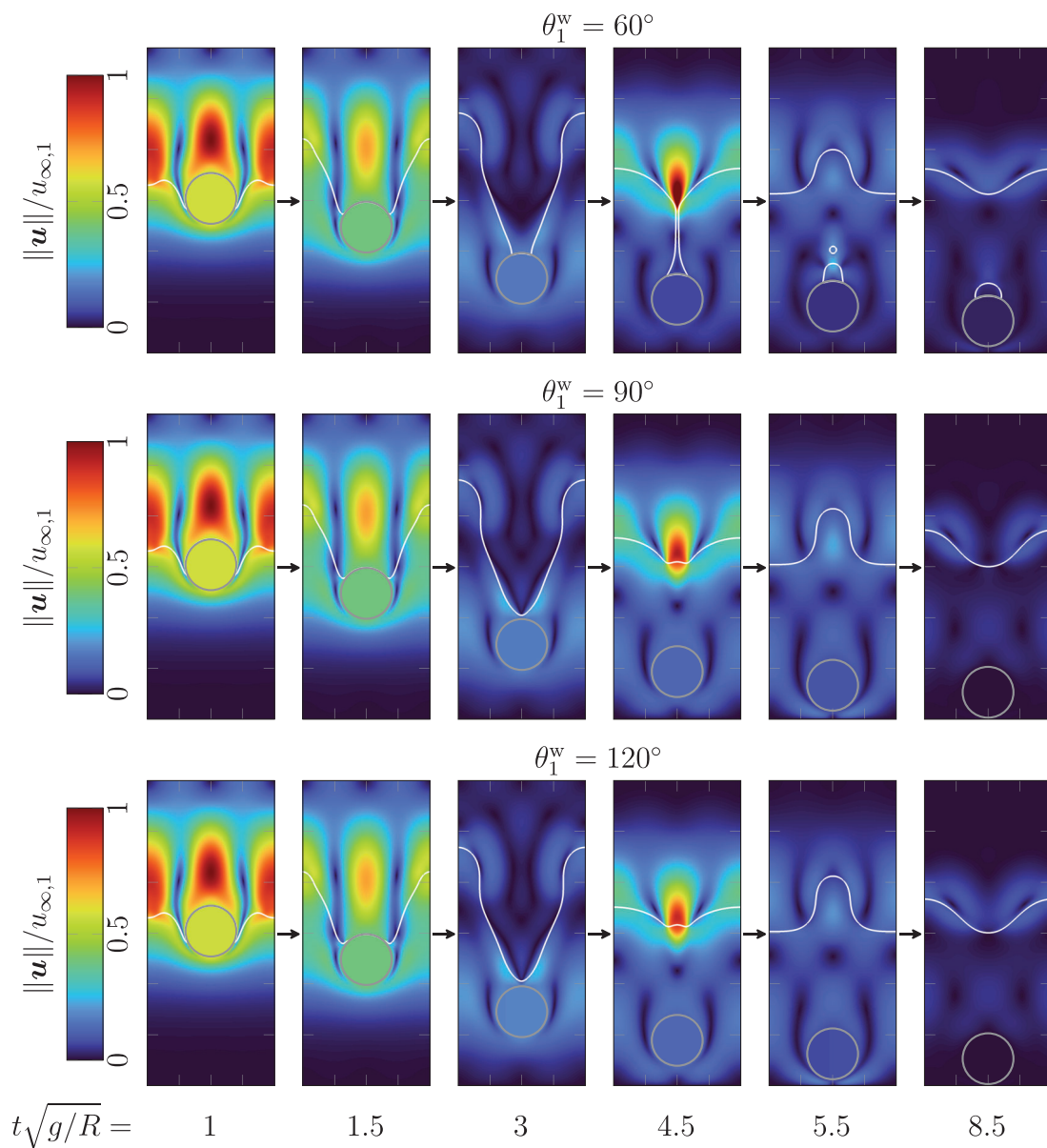

FIGURE 11 Snapshots of the falling sphere simulations for different contact angles. Velocity magnitude and 0.5-iso-lines of φ_1^f (white) and φ^s (gray)

parameters.[19] This droplet induces an additional lift force compared to the other two cases, which leads to a significantly slower sinking of the particle.

In Appendix D a more detailed view on the triple junction region is showed. Additionally, the different behavior of iso-lines with respect to φ_1^f, φ_2^f, and $\tilde{\varphi}$ within the fluid-solid interface is discussed there.

For the same setup and the 90° case, a 3D-simulation with 200 cells in z-direction was conducted in order to show the methods capability to handle three dimensional problems. Figure 12 depicts the phase-field iso-surfaces at different times. Qualitatively, the 3D results show the same behavior as in 2D. The simulation study demonstrates the capability of the present model to capture wetting behavior of moving solid bodies within a two-phase flow.

4.4 | Impact of two spheres involving a solid obstacle structure

We consider a similar setup to the previous Section 4.3 and adjust it in a way, that two spheres drop onto a free surface and an additional solid structure is involved as depicted in Figure 13. Both particles have the same initial velocity similar to the one in Section 4.3. A hard sphere collision model[6] is applied for particle-particle contact and collisions with the solid structure are treated as described in Reference 10. Purely elastic collisions are considered and thus the coefficient of restitution $e = 1$ is chosen. A time series of the simulation is shown in Figure 14. After the lower sphere hits the free surface, it gets decelerated and both spheres collide. Afterwards a contact between the solid structure and the lower sphere leads to repelling to the right. This impact causes the breakup and splash of the dense fluid leading to a droplet moving toward the left wall. This simulation example illustrates the framework's capability in treating complex contact situations of multiple solids within the two-phase flow.
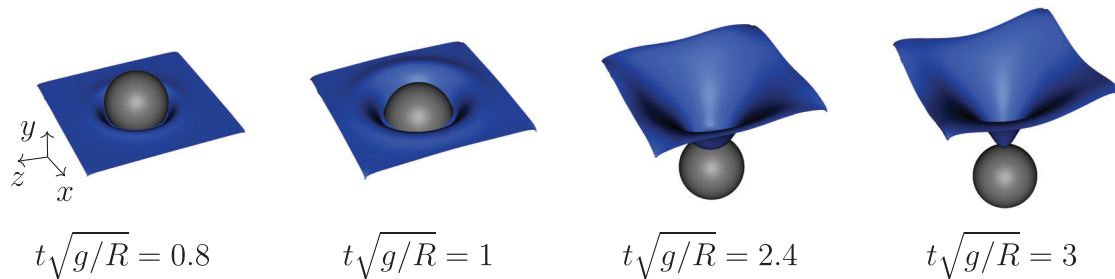

$t\sqrt{g/R} = 0.8$ $t\sqrt{g/R} = 1$ $t\sqrt{g/R} = 2.4$ $t\sqrt{g/R} = 3$

FIGURE 12 Iso-surfaces of $\varphi_1^f = 0.5$ (blue) and $\varphi^s = 0.5$ (gray) for the 3D simulation with $\theta_1^w = 90°$
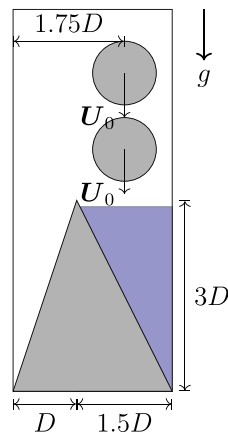

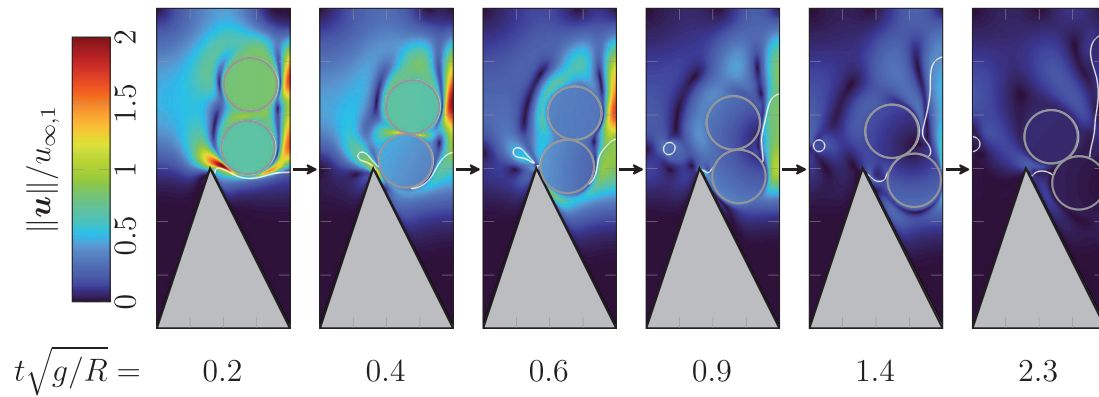**FIGURE 13** Initial setup for the impact on the free surface with a solid structure as obstacle

FIGURE 14 Snapshots of the simulation. Velocity magnitude and 0.5-iso-lines of φ_1^f (white), φ_p (gray) and φ^s (black)
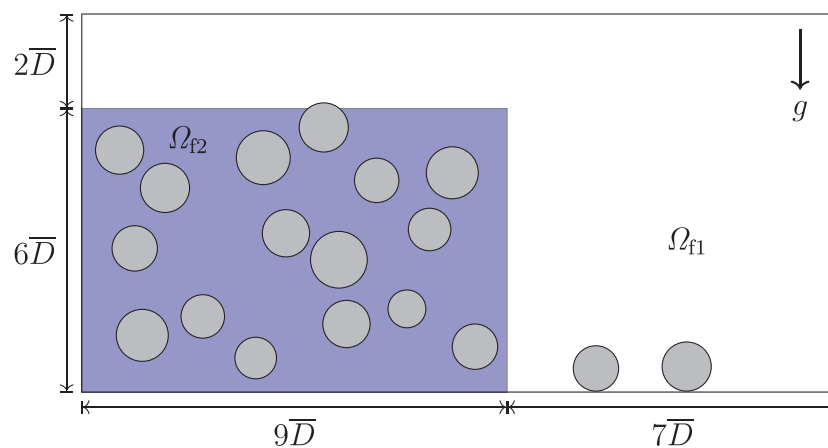

FIGURE 15 Initial setup for the dam breaking problem with immersed spherical bodies

4.5 | Breaking dam problem with rigid particles

In order to show the further capability of the present model and simulation framework to handle multiple particles interacting with two-phase flow, the breaking dam problem sketched in Figure 15 is considered. A number of eighteen differently sized particles are placed into the domain. The mean diameter is $\overline{D} = 0.2$ m and the particle sizes vary within $0.8\overline{D} \leq D_p \leq 1.2\overline{D}$. The boundaries are solid walls where the impermeability and no-slip condition holds. All material parameters and the cell numbers over the interface are identical to the previous section. The coefficient of restitution is chosen as $e = 0$ and a contact angle of 90° is enforced between the fluids and particles as well as at walls. 1280×640 cells are used to discretize the domain and a mobility value of $\kappa = 0.005$ m^3 s kg^{-1} is employed. During the simulation, the maximum blending parameter according to Equation (42) was $\gamma = 0.8$ and thus the discretization of convection in the momentum balance tends more toward UDS. The simulation took 17 hours on a single core of an Intel Xeon E5-2620 processor at 2.1 GHz to reach a time of $t/\sqrt{g/R} \approx 6$ corresponding to 80,000 time steps. Thereby, the calculation time is distributed as 85% for the Navier–Stokes solution and therein mainly the Poisson solver, 13.5% for rigid body projection and the collision algorithm, 0.8% for the normalization procedure and Cahn–Hilliard equation. The rest of the time is required for input/output and so forth.

Figure 16 shows snapshots of the simulation at four different times. The fluid-fluid interface is depicted alongside the rigid particles with their barycenter velocity. The particles are transported within the denser fluid 2 and undergo collisions with each other and the wall. Both, fluid 2 as well as the immersed particles splash onto the right wall and get deflected toward the wall tangential direction y there. Some inclusions of the lighter fluid 1 remain in the vicinity of the right bottom corner.
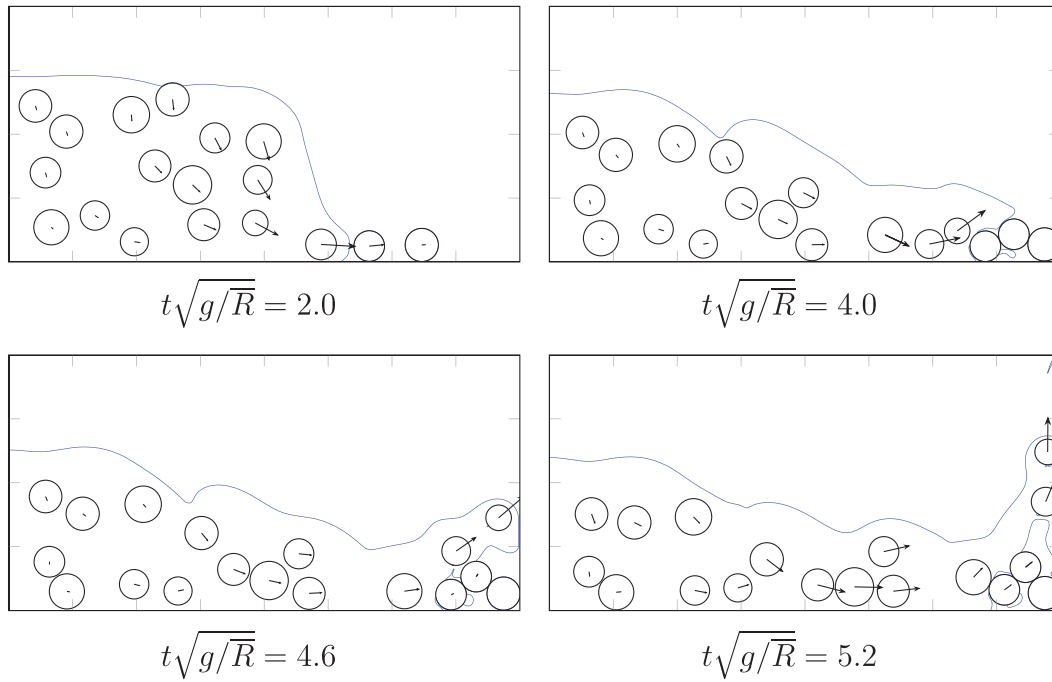
FIGURE 16 Snapshots of the breaking dam simulation. Particles with respective barycenter velocity and 0.5-iso-lines of φ_1^{f} (blue) for different times

This numerical experiment shows, that the presented model is able to treat complex topological changes of the fluid-fluid interface introduced by the motion and interaction of multiple rigid bodies in the flow.

5 | CONCLUSIONS

Within this article, a model for two-phase particulate flow is introduced based on a full multiphase-field approach. It enables the simulation of rigid body movement interacting with two-phase flow by using a single Eulerian configuration without the requirement of body fitted meshes. All occurring interfaces are represented via phase-field order parameters. A normalization procedure enables a decoupling of the two-phase flow on one hand and the rigid particulate flow on the other. The rigid body motion is captured via a distributed Lagrange multiplier method. For the two-phase flow, a Hohenberg–Halperin model with respect to the normalized phase variable is employed. The corresponding boundary conditions are applied over a diffuse fluid-solid interface using the procedure of Li et al..[21] This enables the consideration of contact line dynamics and different wetting behavior on moving solid surfaces according to Young's law. The diffuse wetting boundary condition is shown to reproduce the theoretical contact angle for a droplet on a wall represented by a diffuse fluid-solid interface. Additionally, the overall model is validated on the theoretical solution for the heave decay problem within this article. Different simulation examples are shown, which illustrate the present model's capability to handle two-phase particulate flow in dynamic wetting situations and the interaction with contact problems including multiple rigid bodies and arbitrary solid structures. The present model was implemented with an explicit first order time integration. However, it can be generalized using a more sophisticated scheme for example, similar to the one of Apte et al.[33] in order to enhance temporal accuracy. Additionally, a more efficient multigrid solver for the Poisson equation can yield a significant speed up of the simulations. Both aspects can be subject of future work.

DATA AVAILABILITY STATEMENT

The data that support the findings of this study are available from the corresponding author upon reasonable request.

ORCID

Martin Reder https://orcid.org/0000-0002-7503-9351

REFERENCES

1. Calderer A, Kang S, Sotiropoulos F. Level set immersed boundary method for coupled simulation of air/water interaction with complex floating structures. *J Comput Phys*. 2014;277:201-227.
2. Choi YJ, Anderson PD. Cahn–Hilliard modeling of particles suspended in two-phase flows. *Int J Numer Methods Fluids*. 2012;69(5):995-1015.
3. Ueda Y, Tanaka M, Uemura T, Iguchi M. Water entry of a superhydrophobic low-density sphere. *J Vis*. 2010;13(4):289-292.
4. Liu Z, Mukherjee PP. Microstructure evolution in lithium-ion battery electrode processing. *J Electrochem Soc*. 2014;161(8):E3248-E3258.
5. Basting S, Quaini A, Čanić S, Glowinski R. Extended ale method for fluid–Structure interaction problems with large structural displacements. *J Comput Phys*. 2017;331:312-336.
6. Johnson AA, Tezduyar TE. Simulation of multiple spheres falling in a liquid-filled tube. *Comput Methods Appl Mech Eng*. 1996;134(3-4):351-373.
7. Glowinski R, Pan T-W, Hesla TI, Joseph DD. A distributed Lagrange multiplier/fictitious domain method for particulate flows. *Int J Multiphase Flow*. 1999;25(5):755-794.
8. Patankar NA, Singh P, Joseph DD, Glowinski R, Pan T-W. A new formulation of the distributed Lagrange multiplier/fictitious domain method for particulate flows. *Int J Multiphase Flow*. 2000;26(9):1509-1524.
9. Sharma N, Patankar NA. A fast computation technique for the direct numerical simulation of rigid particulate flows. *J Comput Phys*. 2005;205(2):439-457.
10. Reder M, Schneider D, Wang F, Daubner S, Nestler B. Phase-field formulation of a fictitious domain method for particulate flows interacting with complex and evolving geometries. *Int J Numer Methods Fluids*. 2021;93(8):2486-2507.
11. Jacqmin D. Calculation of two-phase Navier–Stokes flows using phase-field modeling. *J Comput Phys*. 1999;155(1):96-127.
12. Abels H, Garcke H, Grün G. Thermodynamically consistent, frame indifferent diffuse interface models for incompressible two-phase flows with different densities. *Math Models Methods Appl Sci*. 2012;22(03):1150013.
13. Kim J. Phase-field models for multi-component fluid flows. *Commun Comput Phys*. 2012;12(3):613-661.
14. Hohenberg PC, Halperin BI. Theory of dynamic critical phenomena. *Rev Mod Phys*. 1977;49(3):435.
15. Jacqmin D. Contact-line dynamics of a diffuse fluid interface. *J Fluid Mech*. 2000;402:57-88.
16. Malvandi A, Ghasemi A, Nikbakhti R, Ghasemi A, Hedayati F. Modeling and parallel computation of the non-linear interaction of rigid bodies with incompressible multi-phase flow. *Comput Math Appl*. 2016;72(4):1055-1065.
17. Aland S, Lowengrub J, Voigt A. Particles at fluid-fluid interfaces: a new Navier-Stokes-Cahn-Hilliard surface-phase-field-crystal model. *Phys Rev E*. 2012;86(4):046321.
18. Joshi V, Jaiman RK. A hybrid variational Allen-Cahn/ALE scheme for the coupled analysis of two-phase fluid-structure interaction. *Int J Numer Methods Eng*. 2019;117(4):405-429.
19. Li H-L, Liu H-R, Ding H. A fully 3D simulation of fluid-structure interaction with dynamic wetting and contact angle hysteresis. *J Comput Phys*. 2020;420:109709.
20. Aland S, Lowengrub J, Voigt A. Two-phase flow in complex geometries: a diffuse domain approach. *Comput Model Eng Sci CMES*. 2010;57(1):77.
21. Li X, Lowengrub J, Rätz A, Voigt A. Solving PDES in complex geometries: a diffuse domain approach. *Commun Math Sci*. 2009;7(1):81-107.
22. Ding H, Spelt PD, Shu C. Diffuse interface model for incompressible two-phase flows with large density ratios. *J Comput Phys*. 2007;226(2):2078-2095.
23. Sun Y, Beckermann C. Sharp interface tracking using the phase-field equation. *J Comput Phys*. 2007;220(2):626-653.
24. Gal CG, Medjo TT. On a regularized family of models for homogeneous incompressible two-phase flows. *J Nonlinear Sci*. 2014;24(6):1033-1103.
25. Jacqmin D. An energy approach to the continuum surface tension method. Proceedings of the 34th Aerospace sciences meeting and exhibit; 1996:858; AIAA.
26. Hoffrogge P, Mukherjee A, Nani E, et al. Multiphase-field model for surface diffusion and attachment kinetics in the grand-potential framework. *Phys Rev E*. 2021;103(3):033307.
27. Hötzer J, Reiter A, Hierl H, Steinmetz P, Selzer M, Nestler B. The parallel multi-physics phase-field framework PACE3D. *J Comput Sci*. 2018;26:1-12.

28. Waterson NP, Deconinck H. Design principles for bounded higher-order convection schemes–A unified approach. *J Comput Phys*. 2007;224(1):182-207.

29. Maskell S, Ursell F. The transient motion of a floating body. *J Fluid Mech*. 1970;44(2):303-313.

30. Itō S. *Study of the Transient Heave Oscillation of a Floating Cylinder*. PhD thesis. Massachusetts Institute of Technology, 1971.

31. Schiller L, Naumann A. Fundamental calculations in gravitational processing. *Z Ver Dtsch Ing*. 1933;77:318-320.

32. Lee D-G, Kim H-Y. Impact of a superhydrophobic sphere onto water. *Langmuir*. 2008;24(1):142-145.

33. Apte SV, Martin M, Patankar NA. A numerical method for fully resolved simulation (FRS) of rigid particle–Flow interactions in complex flows. *J Comput Phys*. 2009;228(8):2712-2738.

APPENDIX A. DERIVATION OF THE DIFFUSE WETTING CONDITION

The field equation for the phase variable is

$$\Phi = a_2\partial_\varphi\psi - a_1\nabla^2\varphi, \tag{A1a}$$

$$\dot\varphi = \kappa\nabla^2\Phi \tag{A1b}$$

with the boundary conditions

$$\nabla\Phi \cdot \boldsymbol{n} = 0, \tag{A2a}$$

$$a_1\nabla\varphi \cdot \boldsymbol{n} = (\sigma_{2s} - \sigma_{1s})\partial_\varphi h^{\mathrm{ff}}(\varphi), \tag{A2b}$$

for static wetting. Multiplication of the Cahn–Hilliard equation with a test function Ψ and integration over the volume $V \subset \Omega$ yields the weak form

$$\int_V \dot\varphi\Psi + \kappa\nabla\Phi \cdot \nabla\Psi \; \mathrm{d}V - \kappa\int_\Gamma \Psi\nabla\Phi \cdot \boldsymbol{n} \; \mathrm{d}S = 0. \tag{A3}$$

The integral can be extended to the whole domain Ω using the indicator function I and Dirac distribution δ_Γ located at the boundary Γ, which yields

$$\int_\Omega I\dot\varphi\Psi + \kappa I\nabla\Phi \cdot \nabla\Psi \; \mathrm{d}V - \kappa\delta_\Gamma\Psi\nabla\Phi \cdot \boldsymbol{n} \; \mathrm{d}V = 0. \tag{A4}$$

It can be exploited, that

$$\int_\Omega I\nabla\Phi \cdot \nabla\Psi \; \mathrm{d}V = \int_\Omega \nabla \cdot (I\Psi\nabla\Phi) - \Psi\nabla \cdot (I\nabla\Phi) \; \mathrm{d}V. \tag{A5}$$

Since I vanishes at the domain boundary $\partial\Omega$, the first part of the integral drops out after using the Gauß divergence theorem. Thus, we obtain

$$\int_\Omega \Psi \left[I\dot\varphi - \kappa\nabla \cdot (I\nabla\Phi) - \kappa\delta_\Gamma\nabla\Phi \cdot \boldsymbol{n}\right] \; \mathrm{d}V = 0. \tag{A6}$$

In the same manner the chemical potential can be treated. The weak form is

$$\int_V \Phi\Psi - a_1\nabla\varphi \cdot \nabla\Psi - a_2\partial_\varphi\psi\Psi \; \mathrm{d}V + a_1\int_\Gamma \Psi\nabla\varphi \cdot \boldsymbol{n} \; \mathrm{d}S = 0 \tag{A7}$$

and therefore

$$\int_\Omega \Psi \left[I\Phi + a_1 \nabla \cdot (I\nabla\varphi) - a_2 I \partial_\varphi \psi + a_1 \delta_\Gamma \nabla\varphi \cdot \boldsymbol{n} \right] \, \mathrm{d}V = 0. \tag{A8}$$

The fundamental Lemma of variation calculus can be used to retrieve the equations

$$I\Phi = a_2 I \partial_\varphi \psi - a_1 \nabla \cdot (I\nabla\varphi) - a_1 \delta_\Gamma \nabla\varphi \cdot \boldsymbol{n}, \tag{A9a}$$

$$I\dot{\varphi} = \kappa \nabla \cdot (I\nabla\Phi) + \kappa \delta_\Gamma \nabla\Phi \cdot \boldsymbol{n}, \tag{A9b}$$

where the boundary conditions are included via the terms containing the Dirac distribution δ_Γ. Inserting the boundary conditions (A2) yields

$$I\Phi = a_2 I \partial_\varphi \psi - a_1 \nabla \cdot (I\nabla\varphi) - \delta_\Gamma (\sigma_{2s} - \sigma_{1s}) \partial_\varphi h^{\mathrm{ff}}, \tag{A10a}$$

$$I\dot{\varphi} = \kappa \nabla \cdot (I\nabla\Phi). \tag{A10b}$$

The diffuse interface approximation of this is obtained by approximating the indicator function via $I \approx h^{\mathrm{fs}}(\varphi^{\mathrm{f}})$ and the Dirac distribution via $\delta_\Gamma = \|\nabla I\| \approx \partial_{\varphi^{\mathrm{f}}} h^{\mathrm{fs}}(\varphi^{\mathrm{f}}) \|\nabla\varphi^{\mathrm{f}}\|$ and thus

$$h^{\mathrm{fs}}\Phi = a_2 h^{\mathrm{fs}} \partial_\varphi \psi - a_1 \nabla \cdot \left(h^{\mathrm{fs}} \nabla\varphi \right) - \partial_{\varphi^{\mathrm{f}}} h^{\mathrm{fs}} \|\nabla\varphi^{\mathrm{f}}\| (\sigma_{2s} - \sigma_{1s}) \partial_\varphi h^{\mathrm{ff}}, \tag{A11a}$$

$$h^{\mathrm{fs}}\dot{\varphi} = \kappa \nabla \cdot \left(h^{\mathrm{fs}} \nabla\Phi \right). \tag{A11b}$$

APPENDIX B. APPLICATION OF DOMAIN BOUNDARY CONDITIONS FOR THE DISCRETIZED CASE

In order to employ the phase-field boundary conditions at the global domain boundary, they need to be discretized. Therefore, a second order scheme for their application is introduced. We exemplarily show it for the two-dimensional case at the left boundary. The index $i = 1$ denotes the first cell center in x-direction while $i = 0$ refers to a cell center outside the actual domain, where the value is extrapolated in order to fulfill the boundary condition. The left wall, where the boundary conditions should be applied, is at position $i = 1/2$. In the 2D case we obtain the discretized Laplace operator

$$\nabla^2 \tilde{\varphi}|_{1,j} \approx \frac{1}{\Delta x} \left[\frac{\tilde{\varphi}_{2,j} - \tilde{\varphi}_{1,j}}{\Delta x} - \frac{\tilde{\varphi}_{1,j} - \tilde{\varphi}_{0,j}}{\Delta x} \right] + \frac{1}{\Delta y} \left[\frac{\tilde{\varphi}_{1,j+1} - \tilde{\varphi}_{1,j}}{\Delta y} - \frac{\tilde{\varphi}_{1,j} - \tilde{\varphi}_{1,j-1}}{\Delta y} \right].$$

Let $\gamma := (\sigma_{2s} - \sigma_{1s})/a_1$, then the values for $\tilde{\varphi}_{0,j}$ result from the boundary condition

$$\partial_x \tilde{\varphi}|_{1/2,j} = \gamma g_{1/2,j} = \gamma g \left(\frac{\tilde{\varphi}_{1,j} + \tilde{\varphi}_{0,j}}{2} \right), \tag{B1}$$

with the abbreviation $g := \partial_{\tilde{\varphi}} h$. For a choice of interpolation leading to $g = 6\tilde{\varphi}(1 - \tilde{\varphi})$, the discretization yields

$$\frac{\tilde{\varphi}_{1,j} - \tilde{\varphi}_{0,j}}{\Delta x} = \gamma \frac{3}{2} (\tilde{\varphi}_{1,j} + \tilde{\varphi}_{0,j})(2 - \tilde{\varphi}_{1,j} - \tilde{\varphi}_{0,j}) \tag{B2}$$

and the solution with respect to the unknown value $\tilde{\varphi}_{0,j}$ is

$$\tilde{\varphi}_{0,j} = 1 - \tilde{\varphi}_{1,j} + \frac{1}{3\gamma\Delta x} \left[1 - \sqrt{1 + 3\gamma\Delta x(2 - 4\tilde{\varphi}_{1,j} + 3\gamma\Delta x)} \right], \tag{B3}$$

which can be plugged into the formula for $\nabla^2 \tilde{\varphi}|_{1,j}$ yielding $\Phi_{1,j}$. Note, that the second solution of the quadratic equation is not valid, since it would violate the summation constraint. The update for $\tilde{\varphi}$ is

$$\tilde{\varphi}_{1,j}^{n+1} = \tilde{\varphi}_{1,j}^{n} + \kappa \Delta t \left[\frac{\Phi_{2,j} - \Phi_{1,j}}{\Delta x^2} + \frac{\Phi_{1,j+1} - 2\Phi_{1,j} + \Phi_{1,j-1}}{\Delta y^2} \right], \tag{B4}$$

since $\Phi_{0,j+1} = \Phi_{1,j+1}$ holds due to the boundary condition (28).

APPENDIX C. DERIVATION OF THE DROPLET DIMENSIONS

A two-dimensional droplet is shown schematically in Figure C1. A formula for the total area A and a relation between the aspect ratio h/w and angle θ can be derived by simple geometrical arguments. First we note that the lower right-hand triangle shows by trigonometry that

$$r - h = r \cos \theta \tag{C1}$$

$$\frac{w}{2} = r \sin \theta \tag{C2}$$

and hence the aspect ratio

$$\frac{h}{w} = \frac{1 - \cos \theta}{2 \sin \theta} = \frac{1}{2} \tan \frac{\theta}{2}. \tag{C3}$$

The quantity

$$c := \frac{2h}{w} = \tan \frac{\theta}{2} \tag{C4}$$

can be used to calculate the contact angle with known width and height of the droplet. Values of c for typical wetting angles can be found in Table C1.
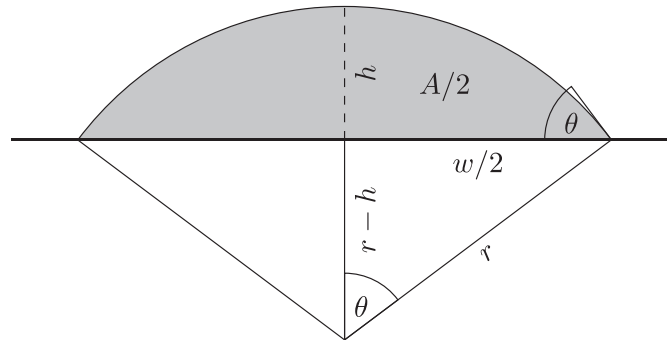

FIGURE C1 A two-dimensional droplet (gray) with total area A under wetting angle θ has dimensions height h and width w in its equilibrium spherical shape of radius r

TABLE C1 Relation between the aspect ratio parameter c and angle θ for a two-dimensional droplet

θ	$c = 2h/w$ (exact)	c (approx)
30°	$2 - \sqrt{3}$	0.267949192
45°	$\sqrt{2} - 1$	0.414213562
60°	$\sqrt{3}/3$	0.577350269
90°	1	1
120°	$\sqrt{3}$	1.7320508

Moreover, the area of the triangle equals $r^2/2 \sin\theta \cos\theta$. Additionally, the right-hand side wedge of angle θ has area $r^2(\theta/2)$. Subtracting the triangle contribution from the wedge yields one half of the total area A as $A/2 = r^2/2\,(\theta - \sin\theta\cos\theta)$, and hence the relation between the size and area of the droplet is given by

$$A = r^2\,(\theta - \sin\theta\cos\theta)\ . \tag{C5}$$

Find a table of values of the simulation results below.

TABLE C2 Simulation results for the droplet wetting behavior

$\theta_1^w = 60°$			$\theta_1^w = 90°$			$\theta_1^w = 120°$		
n_x	c	$\Delta\theta_1^w$	n_x	c	$\Delta\theta_1^w$	n_x	c	$\Delta\theta_1^w$
180	0.53543	3.6679	180	1.01644	−0.934188	180	1.8165	−2.334234
200	0.54481	2.8356	200	1.01420	−0.80796	200	1.8033	−1.979160
220	0.55779	1.6955	220	1.00443	−0.253141	220	1.7941	−1.729712
240	0.56042	1.4658	240	1.00429	−0.245190	240	1.7953	−1.763842
260	0.56684	0.9073	260	0.99734	0.15239	260	1.7673	−0.994074
280	0.57117	0.5328	280	0.99639	0.20743	280	1.7601	−0.794934
$\delta_{fs}/\Delta x$	c	$\Delta\theta_1^w$	$\delta_{fs}/\Delta x$	c	$\Delta\theta_1^w$	$\delta_{fs}/\Delta x$	c	$\Delta\theta_1^w$
2	0.53949	3.3073	2	1.0838	−4.604158	2	1.9432	−5.537363
3	0.54743	2.6048	3	1.0569	−3.168663	3	1.9109	−4.751598
4	0.56222	1.3088	4	1.0030	−0.173025	4	1.8506	−3.229645
5	0.55779	1.6955	5	1.0044	−0.253141	5	1.7941	−1.729712
6	0.57071	0.57192	6	1.0090	−0.510905	6	1.7941	−1.731826
7	0.56839	0.77343	7	1.0206	−1.168453	7	1.7704	−1.0794

Note: Table of values for the plots in Figure 6. Deviation of the contact angle $\Delta\theta_1^w$ in ° and aspect ratio $c = 2l_y/l_x$.

APPENDIX D. DYNAMIC TRIPLE-JUNCTION BEHAVIOR

This section addresses triple-junction dynamics from the simulations in Section 4.3. Figure D1 shows the iso-lines of all phases exemplarily for the second snapshot in Figure 11 of the $\theta_1^w = 90°$ and $\theta_1^w = 120°$ case. It can be seen, that iso-lines corresponding to the non-normalized fluid phases approach the iso-line where $\varphi^s = 0.5$ holds. This is due to an additional decrease of the respective fluid phase arising from gradients in φ^s and thus the total fluid phase. In contrast to this, the iso-line of the normalized phase variable $\tilde\varphi$ does not show such a behavior since it is completely independent of φ^s. However, those parts of the $\tilde\varphi = 0.5$ iso-line, which separate the fluid and solid region show artificial sawtooth behavior. This is due to $\tilde\varphi$ not being defined in pure solid regions. The values there are not used and thus set to -FLOAT_MAX in order to indicate those regions visually. Therefore, the corresponding parts of the iso-line are meaningless. In this work use iso-lines of the actual fluid-phases for visualization, since they also represent the fluid-solid interface correctly.
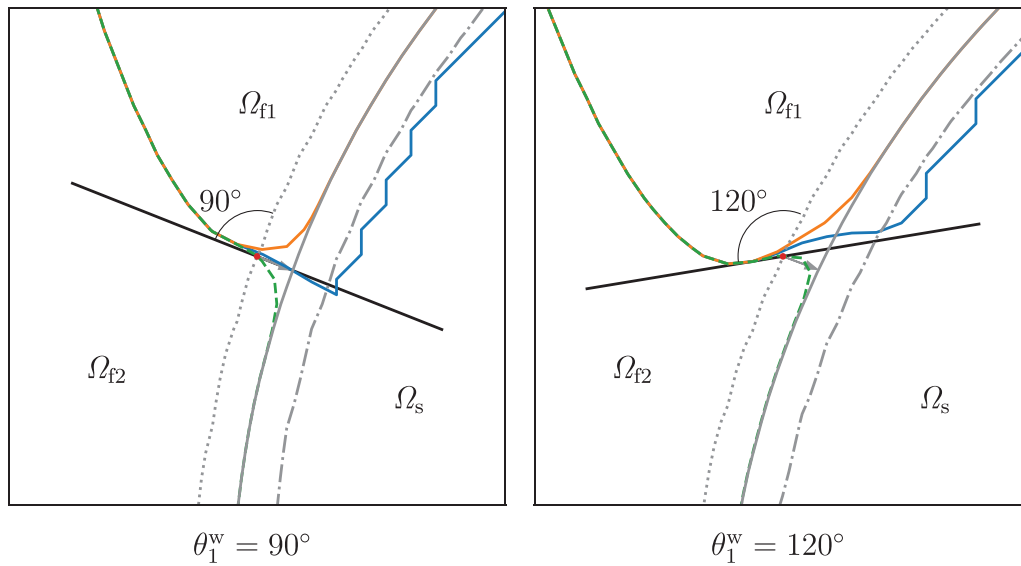
FIGURE D1 Zoomed region close to the triple-junction showing iso-lines from the falling sphere simulations. Green: $\varphi_1^{\mathrm{f}} = 0.5$. Orange: $\varphi_2^{\mathrm{f}} = 0.5$. Blue: $\tilde{\varphi} = 0.5$. Gray: $\varphi^{\mathrm{s}} = 0.1$, $\varphi^{\mathrm{s}} = 0.5$ and $\varphi^{\mathrm{s}} = 0.9$ (dotted, solid, and dashdotted, respectively). Black: Theoretical tangent at $\varphi^{\mathrm{s}} = 0.1$ iso-line for the interface between the two fluids. The arrow indicates the normal on the $\varphi^{\mathrm{s}} = 0.1$ iso-line